SCIENCE CHINA
Technological Sciences

•Article•

November 2022 Vol.65 No.11: 2658–2666
https://doi.org/10.1007/s11431-022-2157-8

Enhanced-performance self-powered photodetector based on multi-layer MoS_2 sandwiched between two asymmetric graphene contacts

GUO JunXiong[1*], LI ShangDong[2], LIN Lin[3], CAI Ji[1], CHEN JianBo[1,4], WANG ShiCai[3], GOU Xin[1], YE JingHua[1], LUO ZhengHua[1,5] & HUANG Wen[3]

[1] *School of Electronic Information and Electrical Engineering, Chengdu University, Chengdu 610106, China;*
[2] *School of Electronics and Information Technology (School of Microelectronics), Sun Yat-sen University, Guangzhou 510006, China;*
[3] *School of Electronic Science and Engineering (National Exemplary School of Microelectronics), University of Electronic Science and Technology of China, Chengdu 610054, China;*
[4] *College of Materials Science and Engineering, Sichuan University, Chengdu 610064, China;*
[5] *Sichuan Time Frequency Synchronization System and Application Engineering Technology Research Center, Chengdu 610062, China*

Received May 26, 2022; accepted July 22, 2022; published online September 28, 2022

Self-powered photodetectors can convert light into electrical signals without external power input and are widely used in applications such as imaging, sensing, communication, and security. The most popular approach for constructing a self-powered photodetector is typically based on the fabrication of an asymmetric metal-semiconductor (MS) contact; however, this technique is seriously limited by the Fermi-level pinning effect. Here, we report a room-temperature photodetector based on multi-layer MoS_2 sandwiched between two separated asymmetric graphene contacts. Our photodetector was driven by the built-in electric field generated by a van der Waals (vdW) contact instead of the traditional MS contact. Operating under zero-bias voltage, the highest photoresponsivity of 0.63 A W^{-1} and a specific detectivity of 7.71×10^{12} Jones were achieved at a wavelength of 450 nm with 0.08 μW cm^{-2} incident power intensity. Compared with devices using symmetric contacts, a high ON/OFF current ratio of approximately 1520 and a fast response time on the order of microseconds were also observed in our asymmetric graphene contact device. Our experimental results may open a novel way toward the realization of vdW contacts for the fabrication of self-powered photodetectors.

MoS_2, graphene, self-powered photodetector, asymmetric contact

Citation: Guo J X, Li S D, Lin L, et al. Enhanced-performance self-powered photodetector based on multi-layer MoS_2 sandwiched between two asymmetric graphene contacts. Sci China Tech Sci, 2022, 65: 2658–2666, https://doi.org/10.1007/s11431-022-2157-8

1 Introduction

Photodetectors, which convert light signals to electrical signals, are widely used in communications [1,2], imaging [3], sensing [4], spectroscopy [5], biomedicine [6], human health [7], and security [8,9], and thus they have become the core technology of our daily lives. To date, numerous photodetectors, including thin-film types (e.g., silicon [5,10,11] and III-V compounds [12]) and novel nanostructured devices (e.g., quantum dots [13], nanowires [14], nanorods, and nanosheets [15]) have reached a mature level because of the increasing development of updated techniques for large-scale production and integration. Recently, many impressive prototype photodetectors based on two-dimensional materials (2DM) and their heterostructures have been developed [16–18] to enrich the range of light detection, mainly owing

*Corresponding author (email: guojunxiong@cdu.edu.cn)

to the unique optical and electronic features of these materials. However, most of these photodetectors require external power input to drive photocarrier separation and photocurrent generation [19–21], which hinders the goal of reducing the device size and weight and limits their application, such as in the wireless and *in situ* detection of wearable and mobile devices. Therefore, an alternative way of producing a photocurrent without external power input, such as the use of asymmetric electrode contacts, should be pursued.

An asymmetric contact [20], which consists of two separated electrodes with different work functions, makes it possible to construct a self-powered photodetector owing to differences in both the Schottky barrier height and the depletion width in the channel between two metal-semiconductor (MS) junctions. The pioneering work to construct an asymmetric contact with 2DM was the integration of graphene with titanium and palladium electrodes [22], which showed a fast switching speed but a low ON/OFF current ratio owing to the large dark current derived from the gapless nature of graphene. Research efforts in asymmetric contact engineering have also focused on other 2DM-based devices for light detection, especially transition metal dichalcogenide (TMD)-layered materials, such as MoS_2 [16,23–25]. Many types of TMD-based self-powered devices using asymmetric contacts have been reported, such as Au-MoS_2-indium tin oxide (ITO) [26], Bi-WS_2-Si [27], and graphene-$MoSe_2$-Au [28]. However, the pinning effect of the Fermi level in these MS contacts significantly limits their photoelectric performance.

van der Waals (vdW) contacts [7,29–31], which are free of MS junctions, offer a promising approach to mediating the pinning effect. In this work, we used two separated asymmetric types of graphene, pristine exfoliated graphene and nitrogen-doped graphene, in contact with multi-layer MoS_2 for self-powered light detection. Our designed device operated at a zero-bias voltage, which was driven by the built-in electric field (E_{in}) in the channel between the two asymmetric graphene/MoS_2 vdW junctions. Our photodetector not only exhibited a high responsivity of 0.63 A W^{-1} and a specific detectivity of 7.71×10^{12} Jones (1 Jones=1 cm $Hz^{1/2}$ W^{-1}) under 450 nm illumination with a power intensity of 0.08 μW cm^{-2} but also a fast response speed on the order of microseconds by fully utilizing the combination of the ultrahigh carrier mobility in graphene and the high light absorption in MoS_2 from visible to near-infrared regimes. We experimentally demonstrate that asymmetric vdW contacts, instead of external power input, can be used to produce a photocurrent and achieve high performance for light detection.

2 Experimental section

2.1 Materials

Both multi-layer MoS_2 and few-layer graphene flakes were obtained using a standard scotch-tape technique for mechanical exfoliation from bulk crystals. Highly oriented pyrolytic graphite and bulk MoS_2 crystals were purchased from SixCarbon Technology (Shenzhen, China). Nitrogen-doped graphene (N-graphene) was obtained using inductively coupled plasma (ICP) treatment with 30 sccm nitrogen flux. The ICP treatment was conducted under a radio frequency (RF) power of 250 W, and the vacuum chamber was pre-evacuated to a pressure of 10^{-4} Pa. The details of the ICP treatment technique can be found in our previous studies [32,33].

2.2 Device fabrication

ITO electrodes 180 nm thick were patterned using a standard photolithography technique combined with chemical wet etching. The exfoliated 2D materials were then transferred onto the patterned ITO electrodes. Finally, to reduce the contact resistance, the fabricated devices were placed in a vacuum oven under a pressure of approximately 30 mTorr (1 Torr=1.33322×10^2 Pa) and annealed for 10 min at 200°C.

We fabricated three different devices: One was MoS_2 in direct contact with bare ITO electrodes, the second was MoS_2 stacked onto two separated graphene layers of the same thickness (symmetric contact), and the third was similar to the second type, but one of the graphene sheets was doped by nitrogen plasma (asymmetric contact), as shown in Figure 1(a).

2.3 Characterization and measurements

In this study, we performed characterization and measurements under ambient and room-temperature conditions. Optical images were obtained using an Olympus BX51M microscope (Japan). Atomic force microscopy (AFM) images and heights were obtained using a Veeco Dimension D3100 AFM instrument (USA). Raman spectra were obtained using a Renishaw micro-Raman spectrometer (UK) with an excitation laser wavelength of 532 nm. The elemental compositions of the materials were determined using an Escalab 250Xi X-ray photoelectron spectrometer (XPS). Current-voltage characteristics were recorded using a Keithley 2400 source meter. For the photocurrent of the device collection, seven lasers with wavelengths of 405, 450, 532, 635, 720, 808, and 980 nm, from the visible to near-infrared range, were used. To avoid the effect of laser-induced heating on our devices, the incident powers of the Raman characterization and the photoelectric performance were controlled to be below 1 mW. The response time was extracted from the current-voltage curves, which were recorded using a Tektronix-TDS 2012C oscilloscope combined with a function signal generator to produce a stable pulsed source.

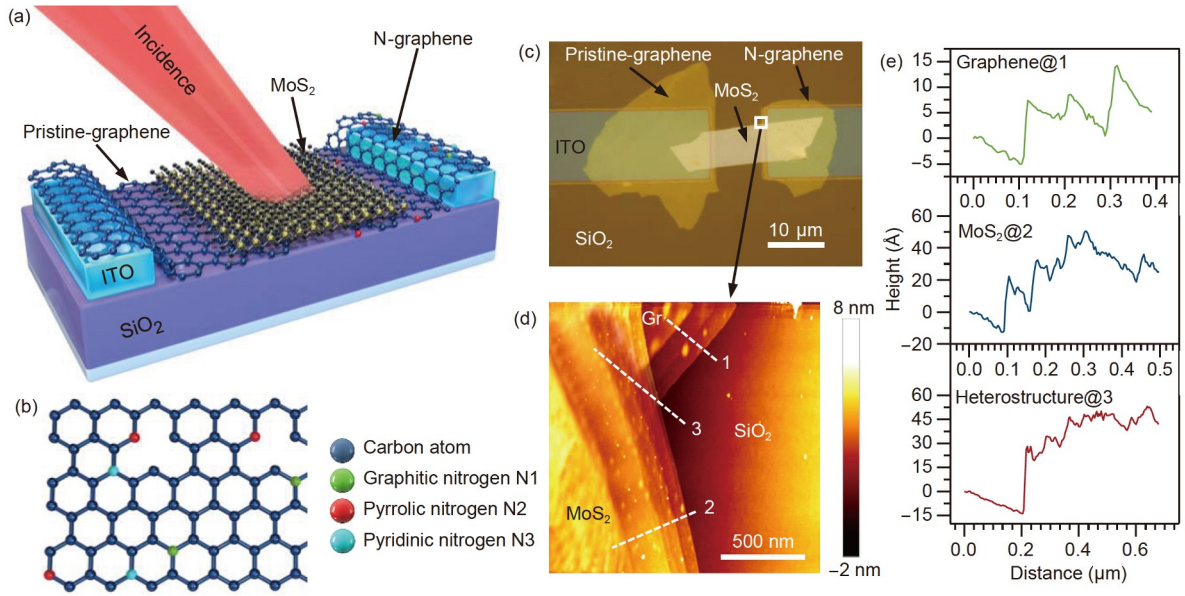

Figure 1 (Color online) Structure of MoS_2 self-powered photodetector using asymmetric graphene contact. Conceptual design of (a) device and (b) proposed structure of N-doped graphene. (c) Optical image (top view) of fabricated device. (d) AFM image of MoS_2/graphene stack on the SiO_2/Si substrate. (e) AFM height plots of different zones of the prepared device. Heights correspond to dashed lines in (d).

3 Results and discussion

3.1 Conceptual design and structure of the device

Our photodetector consisted of a light-absorbing layer of multi-layer MoS_2 flakes stacked between two separate contact layers (Figure 1(a)). The proposed typical structure of N-graphene is illustrated in Figure 1(b). To facilitate the collection of photogenerated carriers and experimentally test the photoelectronic performance, the graphene sheets of the symmetric and asymmetric contact devices were in direct contact with the ITO electrodes. We expected that the introduced graphene layers would accelerate the transfer of photogenerated carriers owing to the excellent electrical properties of graphene. More importantly, the asymmetric contact offers a built-in electric field that allows high-speed and efficient photogenerated carrier separation, enabling the self-powered detection of light without external power input.

Figure 1(c) presents an optical image of our device based on multi-layer MoS_2 stacked with asymmetric graphene contacts (multi-layer MoS_2 sandwiched between pristine graphene and nitrogen-doped graphene). To investigate the enhanced performance of our designed device, we also fabricated two other devices, one based on multi-layer MoS_2 stacked on symmetric graphene (two exfoliated pristine graphene sheets) and one based on bare ITO electrodes (see Figure S1 in Supporting Information). Figure 1(d) shows the AFM image of our fabricated MoS_2 self-powered photodetector, which corresponds to the area enclosed by the solid line in Figure 1(c). The AFM height plots (Figure 1(e), corresponding to the dashed lines in Figure 1(d)) revealed that the thicknesses of bare MoS_2, bare graphene, and their stacks were approximately 42, 13, and 52 Å, respectively, which suggests that the exfoliated MoS_2 and graphene had approximately eight and three layers, respectively.

The compositions of the prepared materials were characterized by monitoring the Raman shifts. For graphene, two principal bands designated as G and 2D bands can be characterized in a relatively simple way. The third band of the D band may also be present owing to the presence of lattice defects within the graphene. Figure 2(a) shows the typical Raman shifts of the prepared graphene sheets. The position of the G band (POG) of the exfoliated pristine graphene is 1583.6 cm^{-1}, suggesting that the thickness of the prepared graphene was three layers according to the following relation [34]:

$$\omega_G = 1581.6 + \frac{11}{1+N^{1.6}}\ (cm^{-1}), \quad (1)$$

where ω_G and N represent the POG and the number of layers of graphene, respectively. In addition, the intensity ratio of 0.84 between the 2D and G bands (I_{2D}/I_G) further confirms that there were three layers of the prepared graphene. These observations are in good agreement with the AFM characterization results (Figure 1(d), (e)). After doping with nitrogen plasma, the intensity ratio between the D and G bands (I_D/I_G) of 0.18 suggests that lattice defects were present within graphene [35]. For MoS_2, the difference in the position between the two principle bands (E_{2g}^1 and A_{1g} bands), Δ, can be used as an index of the number of layers [36]. Two strong peaks were observed within the obtained MoS_2 flakes, and the Δ of the MoS_2 flakes was approximately equal to that of the bulk crystals. Thus, the precise thickness was examined by using the AFM results (Figure 1(d), (e)).

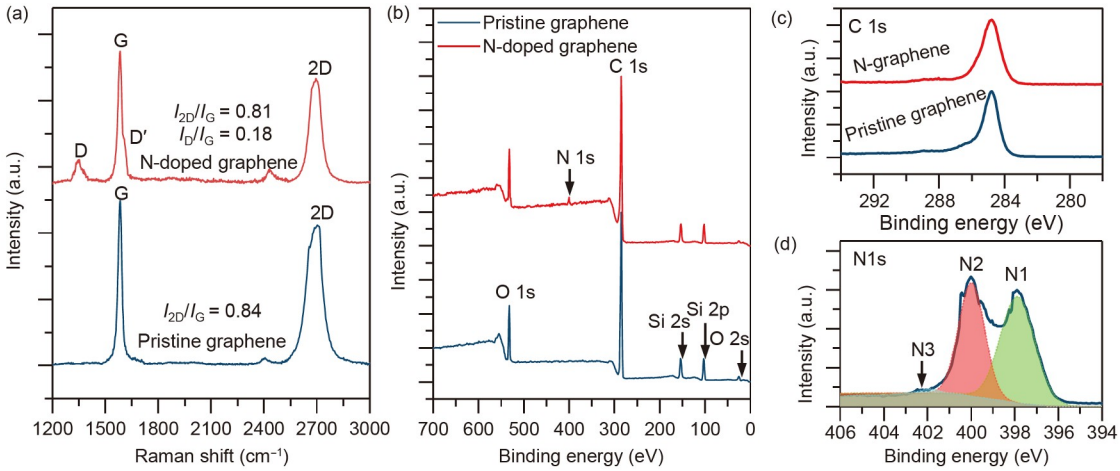

Figure 2 (Color online) Composition of asymmetric graphene contact. (a) Raman shifts of pristine graphene and N-doped graphene. (b) XPS spectra of pristine graphene and N-doped graphene. (c) C 1s XPS spectra of pristine graphene and N-doped graphene. (d) N 1s XPS spectrum of N-doped graphene. N1, N2, and N3 represent the graphitic N, pyrrolic N, and pyridinic N, respectively. The N-doped graphene was obtained using nitrogen plasma treatment.

Next, the elemental compositions of graphene before and after doping were measured using XPS. Figure 2(b) shows predominant C 1s peaks at 284.2 eV, with narrow bands present within both the pristine graphene and the N-graphene. There is also a weak N 1s peak at 400 eV within the N-graphene. As shown in Figure 2(c), the bandwidth of C 1s in N-graphene is softened, mainly referring to the presentation of the C-N bonding energy, compared with that of pristine graphene [37,38]. Figure 2(d) presents the detailed binding energies of the N 1s peaks of N-graphene, which reveal the efficient nitrogen plasma-assisted doping of graphene. The fitting peaks (light-colored peaks) are in good agreement with our proposed structure, shown in Figure 1 (b).

3.2 *I-V* characteristics and the self-powered detection mechanism

Before exploring the photoelectric performance, we first measured the current-voltage (*I-V*) characteristics of MoS_2-based devices using symmetric graphene and asymmetric graphene contacts. Figure 3 presents the source-drain current (I_{ds}) dependence of the bias voltage (V_{ds}) in the two types of devices. Two plots under dark and light illumination cross at V_{ds}=0 in the device using the symmetric graphene contact, as shown in Figure 3(a). This indicates that the built-in electric field (E_{in}) of the channel between the two symmetric graphene contacts was 0. In comparison, in the device using the two separated asymmetric graphene contacts, the two plots under dark and light illumination cross at V_{ds}=−90 mV (Figure 3(b)).

To better understand the working mechanism of our device, the band profiles are schematically presented in the insets of Figure 3, corresponding to the *I-V* characteristics. The difference in the bias voltage at the cross, ΔV_{ds}=−90 mV, indicates that we should apply the bias voltage to offset E_{in} induced by the asymmetric graphene to achieve a flat band profile and zero current. This result is in agreement with our expected design. Based on the above experiments, the potential height in the channel between pristine and N-doped graphene was estimated to be 90 meV. In other words, our designed asymmetric graphene contact makes it possible to self-power the device using a large built-in electric field.

3.3 Photoelectric performance of device

To evaluate the photoelectric performance of our device, we first examined the *I-V* characteristic dependence of the incident power intensity and the corresponding time-resolved source-drain current, and the results are shown in Figure 4 (a)–(c). Under 450-nm laser illumination, the photocurrent increases with increasing input laser power intensity from 0.08 to 16 μW cm^{-2}. The highest short-circuit current density (J_{SC}) of approximately 7.2 μA cm^{-2} is recorded under the operation of zero-bias voltage. Figure 4(d) shows the self-powered mechanism of our designed device, that is, the photovoltage (V_{ph}) generated in the channel between the two asymmetric graphene layers instead of the external bias voltage to produce the photocurrent (I_{ph}). The photocurrent from our device presents a good linear relationship with the incident power intensity (see Figure 4(e)), which is different from a previous report on a MoS_2-graphene hybrid transistor using a single graphene contact [39]. From these experimental results, our designed device follows traditional phototransistor behavior.

We also calculated the photoresponsivity (R_{ph}) of our designed device using eq. (2) [17], where P_{in} and A represent the incident power intensity and active area of the device, respectively. The specific detectivity (D^*) represents the detection limit of a device, which can be described by eq. (3),

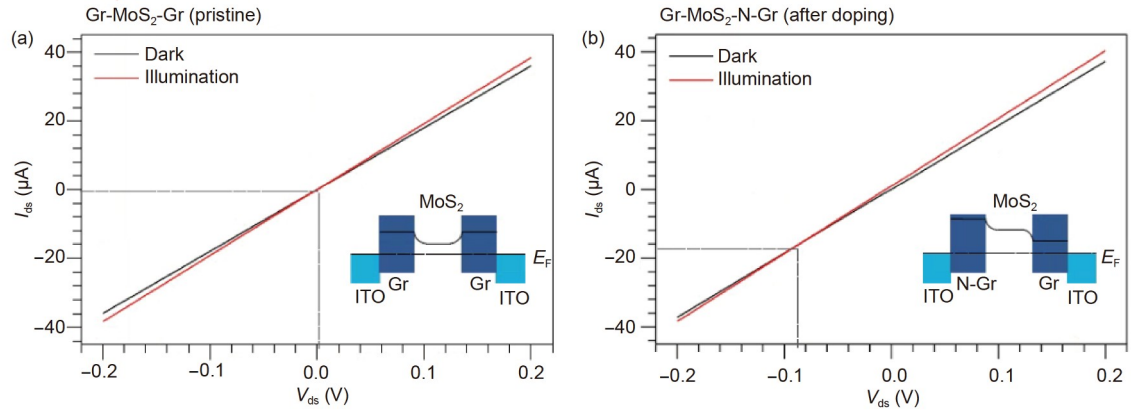

Figure 3 (Color online) Typical *I-V* characteristics of the devices. Source-drain current dependence of the bias voltage in the MoS_2 devices using (a) symmetric graphene contact and (b) asymmetric graphene contact under dark and light illumination. The incident laser wavelength was 450 nm, and the incident power intensity was 0.08 μW cm^{-2}. The insets represent the proposed band alignments of the devices in an equilibrium state.

where I_{dark} is the dark current [17]. From Figure 4(f), under 450-nm laser illumination, we obtained a photoresponsivity of 0.45–0.63 A W^{-1} and a detectivity of 4.62×10^{11} to 7.71×10^{12} Jones by changing the incident power intensity from 0.08 to 16 μW cm^{-2} at zero-bias voltage.

$$R_{ph}=\frac{\text{Photocurrent}}{\text{Incident power}}=\frac{I_{ph}}{P_{in}A}, \tag{2}$$

$$D^{*}=R_{ph}\left(\frac{A}{2eI_{dark}}\right)^{\frac{1}{2}}. \tag{3}$$

Furthermore, the photoelectric performance dependence of the incident wavelength was also investigated. Figure 5(a) presents the time-resolved source-drain current plots under different wavelengths from 405 to 980 nm with the same incident power intensity of 16 μW cm^{-2}. The plots exhibit a broadband photoresponse across the visible spectrum to the near-infrared regime. The corresponding highest photoresponsivity and specific detectivity reached 0.04–0.45 A W^{-1} and 1.54×10^{11} to 4.62×10^{11} Jones, respectively, under the operation of zero-bias voltage (Figure 5(b)).

The external quantum efficiency (EQE) is usually used to investigate the photon-to-electron conversion efficiency of a device, which follows the formula:

$$\text{EQE}=\frac{N_C}{N_I}=R_{ph}\frac{hc}{e\lambda}, \tag{4}$$

where N_C, N_I, h, c, e, and λ represent the collected charge carrier number, incident photon number, Planck's constant, light speed, elementary electron charge, and incident wavelength, respectively [18]. Because of the close relationship between R_{ph} and EQE, Figure 5(b) shows that our device exhibited an EQE as high as 138% under light illumination at 450 nm at zero-bias voltage. However, the EQE of the device decreased to below 10% when the incident wavelength was changed to 980 nm, which was mainly because of the limitation of the intrinsic bandgap of MoS_2.

Next, we focused on the ON/OFF current ratio characteristics of our three devices. The source-drain current curves as a function of time and their corresponding response times extracted from the ON/OFF current ratio plots are shown in Figure 6(a) and (b). For the device using symmetric ITO contacts operating at V_{ds}=0.1 V, the figure shows a high current ON/OFF current ratio (I_{ON}/I_{OFF}) of 133 but a slow response time with increasing time (t_r, interval from 10% to 90% of the maximum photocurrent) of 0.23 s and a fall time (t_f, interval from 90% to 10% of the maximum photocurrent) of 0.55 s. In comparison, we achieved fast response times of t_r=1.2 ms and t_f=2.1 ms when the symmetric graphene contact was used, which may be attributed to the ultrahigh carrier mobility of graphene. However, the symmetric graphene contact-based device exhibits a smaller ON/OFF current ratio (67) than the bare symmetric ITO contact (133). This is reasonable, mainly because of the large dark current in the symmetric graphene contact-based device in which pristine graphene is dominated by the high carrier density and intrinsic zero bandgap. Our designed asymmetric graphene contact exhibited a low dark current and ultrahigh ON/OFF current ratio of approximately 1520 and ultra-fast response times of t_r=26 μs and t_f=50 μs. The low dark current is derived from the zero photovoltage produced under dark conditions (see Figure 3(b)), which is quite different from traditional photodetectors operating under external power input. The fast switching speed is because our device has an ultrahigh ON/OFF current ratio driven by the high built-in electric field between two separated asymmetric graphene layers. These attractive characteristics of the ON/OFF current ratio presented in our designed MoS_2 photodetector using an asymmetric graphene contact provide great potential for numerous applications, such as fast optical communication, optical logic circuits, and imaging systems.

To further enhance the performance of our designed photodetector based on multi-layer MoS_2 stacked with asym-

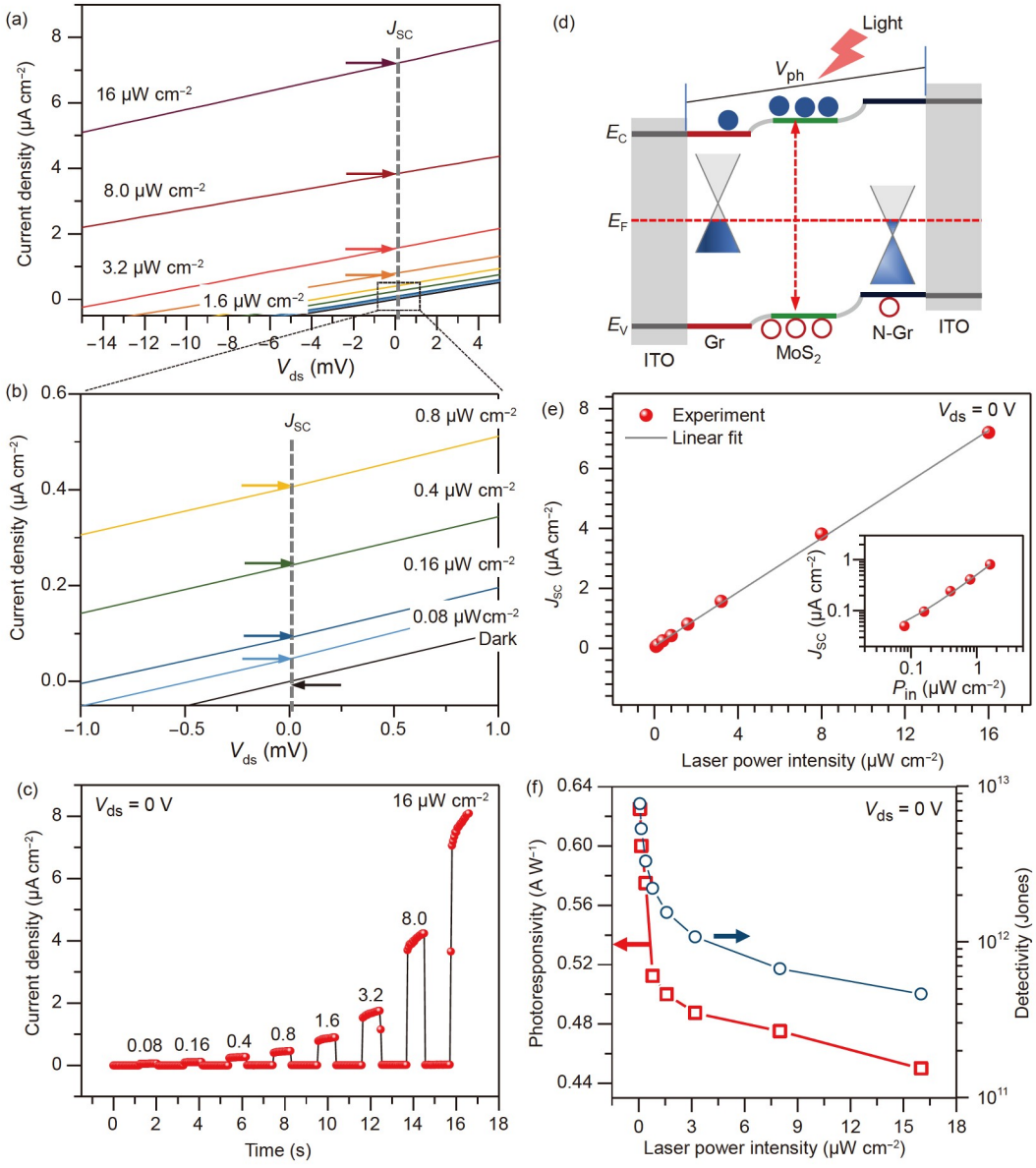

Figure 4 (Color online) Incident power intensity dependence of photoresponse of MoS_2 device using asymmetric graphene contact. (a) Source-drain current dependence of the bias voltage with different incident power intensities and (b) corresponding enlarged views. Dashed lines indicate short-circuit current (V_{ds}=0 V). (c) Time-resolved source-drain current dependence of bias voltage with incident power intensity from 0.08 to 16 μW cm^{-2}. (d) Proposed band alignment of device under illumination. (e) Photocurrent and (f) photoresponsivity, and specific detectivity as functions of incident power intensity under zero-bias voltage. The inset in (e) is the enlarged view of laser power intensity from 0.08 to 1.6 μW cm^{-2}. The solid lines in (e) represent the linear-fitting results. All these experiments were performed under 450-nm laser illumination.

metric graphene, we also investigated the detection performance of the other two types of devices based on multi-layer MoS_2 integrated with symmetric graphene and bare ITO electrodes, respectively. As shown in Figure S2, the photoresponsivity of the three types of devices remained on the same scale owing to the same thickness of the active light absorber of multi-layer MoS_2. However, our designed photodetector using asymmetric graphene contacts achieved enhanced specific detectivity compared to the other two types of devices (see Figure S3). The highest specific detectivities obtained in the devices using asymmetric graphene, symmetric graphene, and bare ITO electrodes were 7.71×10^{12}, 3.74×10^{11}, and 6.27×10^{11} Jones, respectively. From eq. (3), we can see that the enhanced specific detectivity is mainly determined by the low dark current in the device using asymmetric graphene, which agrees with the ultrahigh ON/OFF current ratio (see Figure 6(a)).

Finally, the stability of the device was investigated using extended duration photocurrent measurements. Figure 6(c) shows that the current plots of our device under ON/OFF states using asymmetric graphene contacts remain constant over 5000 cycles of continuous operation upon periodic

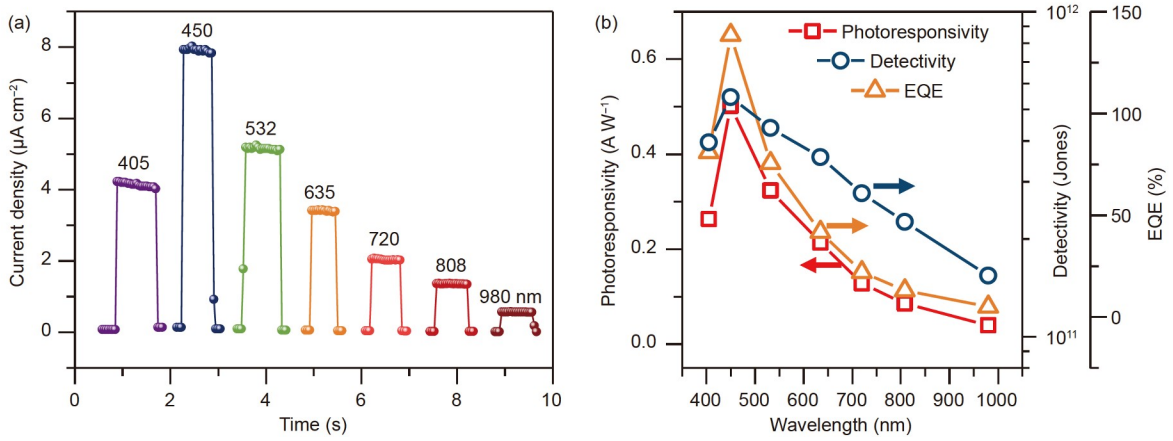

Figure 5 (Color online) Incident wavelength dependence of photoresponse of MoS_2 device using asymmetric graphene contact. (a) Time-resolved source-drain current dependence of bias voltage with the incident wavelength from 405 to 980 nm. (b) Photoresponsivity, specific detectivity, and EQE as a function of incident wavelength under zero-bias voltage. All these cases were performed under a power intensity of 16 μW cm^{-2}.

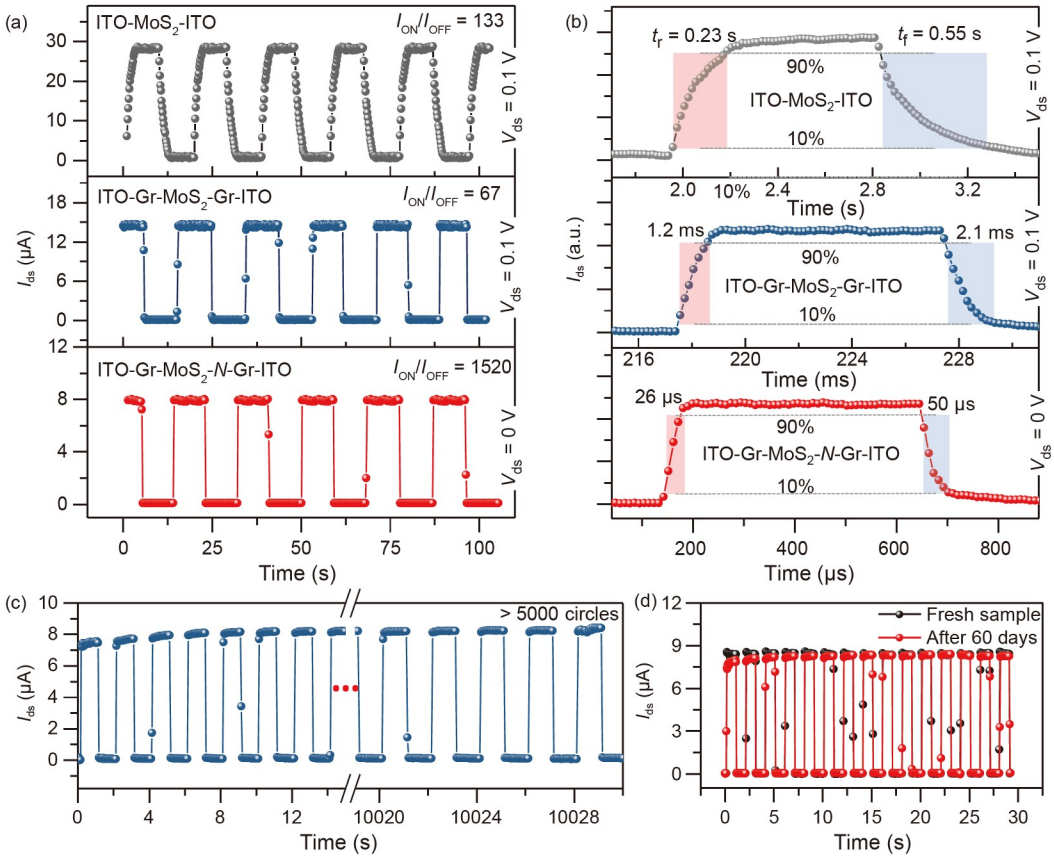

Figure 6 (Color online) Response time and stability of devices. (a) Time-resolved source-drain current dependence of bias voltage with symmetric ITO, symmetric, and asymmetric graphene contacts and (b) related response time. Devices using ITO and symmetric and asymmetric graphene contacts were fabricated under bias voltages of 0.1, 0.1, and 0 V, respectively. (c) The stability of the photoresponse over 5000 cycles. (d) Comparison of the fresh state and after 60 days operation for the device using asymmetric graphene contact.

switching of a 450-nm laser under zero-bias voltage. The photocurrent of our device decreased by less than 5% after exposure to ambient conditions for 60 days compared with that of the fresh sample (Figure 6(d)). The low current loss of the aged device was mainly because of the intrinsic chemical stability of both MoS_2 and graphene [40–43]. These experimental observations demonstrate that the fabricated photodetector exhibits good stability.

4 Conclusions

In summary, we have demonstrated a self-powered photodetector by stacking multi-layer MoS_2 with two separate asymmetric graphene contacts. Raman and XPS measurements confirmed that plasma-assisted treatment could be readily used for doping graphene to form N-graphene. Our designed device operated at a zero-bias voltage (self-powered mode) with high performance because of the high built-in electric field in the channel between the two separated asymmetric graphene contacts. Owing to the working mechanism of the photovoltage-powered device, it exhibited a low dark current and ultrahigh ON/OFF current ratio of approximately 1520 and a fast switching speed on the order of microseconds. A broadband photoresponse from the visible spectrum to the near-infrared regime was also achieved. The highest photoresponsivity of 0.63 A W^{-1} and a specific detectivity of 7.71×10^{12} Jones were recorded under 450-nm laser illumination with a power intensity of 0.08 μW cm^{-2} operating at zero-bias voltage. These merits, along with the maturing technique for the synthesis of 2D materials, may pave the way for the development of novel optoelectronic devices with low energy consumption and large-scale production.

This work was supported by the National Natural Science Foundation of China (Grant No. 61971108), and Science and Technology Foundation of Sichuan Province (Grant No. 2021YFS0311). We thank the Micro & Nano Device Research Center of the University of Electronic Science and Technology of China and the Ceshigo Research Service for their support with the characterizations. We would like to thank Editage (www.editage.cn) for English language editing.

Supporting Information

The supporting information is available online at tech.scichina.com and link.springer.com. The supporting materials have been published as submitted, without typesetting or editing. The responsibility for scientific accuracy and content remains with the authors.

1 Pospischil A, Humer M, Furchi M M, et al. CMOS-compatible graphene photodetector covering all optical communication bands. Nat Photon, 2013, 7: 892–896
2 Mueller T, Xia F, Avouris P. Graphene photodetectors for high-speed optical communications. Nat Photon, 2010, 4: 297–301
3 Mennel L, Symonowicz J, Wachter S, et al. Ultrafast machine vision with 2D material neural network image sensors. Nature, 2020, 579: 62–66
4 Liu J, Dai J, Chin S L, et al. Broadband terahertz wave remote sensing using coherent manipulation of fluorescence from asymmetrically ionized gases. Nat Photon, 2010, 4: 627–631
5 Yu M, Okawachi Y, Griffith A G, et al. Silicon-chip-based mid-infrared dual-comb spectroscopy. Nat Commun, 2018, 9: 1869
6 Rodrigo D, Limaj O, Janner D, et al. Mid-infrared plasmonic biosensing with graphene. Science, 2015, 349: 165–168
7 Lin Z, Huang Y, Duan X. Van der Waals thin-film electronics. Nat Electron, 2019, 2: 378–388
8 Rogalski A, Antoszewski J, Faraone L. Third-generation infrared photodetector arrays. J Appl Phys, 2009, 105: 091101
9 Rogalski A. Infrared detectors: Status and trends. Prog Quantum Electron, 2003, 27: 59–210
10 Lin H, Luo Z, Gu T, et al. Mid-infrared integrated photonics on silicon: A perspective. Nanophotonics, 2018, 7: 393–420
11 Paniccia M, Morse M, Salib M. Silicon Photonics. Berlin: Springer, 2004
12 Lei W, Antoszewski J, Faraone L. Progress, challenges, and opportunities for HgCdTe infrared materials and detectors. Appl Phys Rev, 2015, 2: 041303
13 Tang X, Ackerman M M, Chen M, et al. Dual-band infrared imaging using stacked colloidal quantum dot photodiodes. Nat Photon, 2019, 13: 277–282
14 Sun J, Han M, Gu Y, et al. Recent advances in group III-V nanowire infrared detectors. Adv Opt Mater, 2018, 6: 1800256
15 Konstantatos G, Sargent E H. Nanostructured materials for photon detection. Nat Nanotech, 2010, 5: 391–400
16 Xie C, Mak C, Tao X, et al. Photodetectors based on two-dimensional layered materials beyond graphene. Adv Funct Mater, 2017, 27: 1603886
17 Koppens F H L, Mueller T, Avouris P, et al. Photodetectors based on graphene, other two-dimensional materials and hybrid systems. Nat Nanotech, 2014, 9: 780–793
18 Long M, Wang P, Fang H, et al. Progress, challenges, and opportunities for 2D material based photodetectors. Adv Funct Mater, 2019, 29: 1803807
19 Zhou W, Shang Y, García de Arquer F P, et al. Solution-processed upconversion photodetectors based on quantum dots. Nat Electron, 2020, 3: 251–258
20 Wang Q, Zhou C, Chai Y. Breaking symmetry in device design for self-driven 2D material based photodetectors. Nanoscale, 2020, 12: 8109–8118
21 Tian W, Wang Y, Chen L, et al. Self-powered nanoscale photodetectors. Small, 2017, 13: 1701848
22 Xia F, Mueller T, Lin Y M, et al. Ultrafast graphene photodetector. Nat Nanotech, 2009, 4: 839–843
23 Ponraj J S, Xu Z Q, Chander Dhanabalan S, et al. Photonics and optoelectronics of two-dimensional materials beyond graphene. Nanotechnology, 2016, 27: 462001
24 Butler S Z, Hollen S M, Cao L, et al. Progress, challenges, and opportunities in two-dimensional materials beyond graphene. ACS Nano, 2013, 7: 2898–2926
25 Gupta A, Sakthivel T, Seal S. Recent development in 2D materials beyond graphene. Prog Mater Sci, 2015, 73: 44–126
26 Gong F, Fang H, Wang P, et al. Visible to near-infrared photodetectors based on MoS_2 vertical Schottky junctions. Nanotechnology, 2017, 28: 484002
27 Yao J, Zheng Z, Shao J, et al. Promoting photosensitivity and detectivity of the Bi/Si heterojunction photodetector by inserting a WS_2 layer. ACS Appl Mater Interfaces, 2015, 7: 26701–26708
28 Liu B, Zhao C, Chen X, et al. Self-powered and fast photodetector based on graphene/$MoSe_2$/Au heterojunction. Superlattices Microstruct, 2019, 130: 87–92
29 Novoselov K S, Mishchenko A, Carvalho A, et al. 2D materials and van der Waals heterostructures. Science, 2016, 353: aac9439
30 Geim A K, Grigorieva I V. van der Waals heterostructures. Nature, 2013, 499: 419–425
31 Liu Y, Weiss N O, Duan X, et al. van der Waals heterostructures and devices. Nat Rev Mater, 2016, 1: 16042
32 Ye X, Zhou H, Levchenko I, et al. Low-temperature synthesis of graphene by ICP-assisted amorphous carbon sputtering. ChemistrySelect, 2018, 3: 8779–8785
33 Ke Y, Zhang Z, Guo J, et al. Coexistence of bipolar non-volatile and threshold volatile resistive switching in MoS_2 nanosheets treated by soft nitrogen plasma. Appl Phys Express, 2019, 12: 126507
34 Wang H, Wang Y, Cao X, et al. Vibrational properties of graphene and graphene layers. J Raman Spectrosc, 2009, 40: 1791–1796
35 Kudin K N, Ozbas B, Schniepp H C, et al. Raman spectra of graphite

oxide and functionalized graphene sheets. Nano Lett, 2008, 8: 36–41
36 Lv R, Robinson J A, Schaak R E, et al. Transition metal dichalcogenides and beyond: Synthesis, properties, and applications of single- and few-layer nanosheets. Acc Chem Res, 2015, 48: 56–64
37 Akada K, Terasawa T, Imamura G, et al. Control of work function of graphene by plasma assisted nitrogen doping. Appl Phys Lett, 2014, 104: 131602
38 Wang C D, Yuen M F, Ng T W, et al. Plasma-assisted growth and nitrogen doping of graphene films. Appl Phys Lett, 2012, 100: 253107
39 Li X, Wu J, Mao N, et al. A self-powered grapheme-MoS_2 hybrid phototransistor with fast response rate and high on-off ratio. Carbon, 2015, 92: 126–132
40 Chhowalla M, Shin H S, Eda G, et al. The chemistry of two-dimensional layered transition metal dichalcogenide nanosheets. Nat Chem, 2013, 5: 263–275
41 Wang Q H, Kalantar-Zadeh K, Kis A, et al. Electronics and optoelectronics of two-dimensional transition metal dichalcogenides. Nat Nanotech, 2012, 7: 699–712
42 Zhu Y, Murali S, Cai W, et al. Graphene and graphene oxide: Synthesis, properties, and applications. Adv Mater, 2010, 22: 3906–3924
43 Meyer J C, Geim A K, Katsnelson M I, et al. The structure of suspended graphene sheets. Nature, 2007, 446: 60–63